Article

Correlations and Asymptotic Behaviors of the Shape Parameters of Floating Bubbles Using an Improved Numerical Procedure

Geum-Su Yeom

Department of Mechanical Engineering, Kunsan National University, Gunsan 54150, Korea;
gsyeom@kunsan.ac.kr; Tel.: +82-10-3474-5082

Abstract: An improved numerical procedure is used to present the correlations between the shape parameters and Bond numbers of floating bubbles for a wider range of Bond numbers ($5 \times 10^{-5} < Bo < 5000$) than the previously reported range of Bond numbers ($0.003 < Bo < 241$), and their asymptotic relations as $Bo \to 0$ and $Bo \to \infty$. The proposed method is proven to be more precise and robust than the conventional methods in comparison with previous numerical and experimental results. In addition, the profile of floating bubbles and the related parameters are presented for a wide range of bubble sizes. The shape parameters are divided into three distinct Bond number regions, and are fitted with a fifth-order polynomial as a function of Bond number on a log-log scale for each region. The parameters show two asymptotes, which can be expressed in a simple power law. In addition, the dimensionless maximum depth of the floating bubble is obtained as $H = 0.7291015$ when $Bo = 4.755563$. These correlations and asymptotic relations are expected to assist in the development of scale models of dynamic bubble-related phenomena such as bubble bursting.

Keywords: floating bubble; shape parameter; Bond number; asymptotic relation; power law; Young–Laplace equation

1. Introduction

Bubbles floating on a liquid can be seen in various places, and an understanding of the related phenomena is important in the natural sciences and industrial fields. For example, the bursting of floating bubbles in the ocean affects atmospheric circulation and marine pollution [1–4]. In a nuclear power plant accident, the bursting of bubbles in the reactor acts as a source of radionuclides [5,6]. Volcanic eruptions are caused by bubbles with sizes measured in meters [7]. In food engineering, bubbles are involved in the release of foams and flavors, e.g., champagne, espresso, and beer [8–11]. Recently, boiling heat transfer in a complex nanofluid is closely related to bubble nucleation and growth [12,13].

Bubbles generated in a liquid rise due to buoyancy, and then burst after reaching the liquid surface [14]. Bubbles floating on a liquid can remain in quasi-equilibrium for some time before bursting. During this time, the thin liquid film that defines the surface of the bubble gradually becomes thinner and unstable due to gravity, external disturbance, and impurities [15]. After bursting, the dynamics of the bubble cannot be simulated by the present numerical method, and the partial differential equations of the conservation laws must be solved using the computational fluid dynamics techniques such as the finite element method [16], the arbitrary Lagrangian–Eulerian moving mesh method [17], the two-fluid two-phase flow model [18,19], and the adaptive multi-phase method [20]. As shown schematically in Figure 1, the shape of the floating bubbles in the quasi-equilibrium state can be divided into three curves, namely the cap, the cavity, and the meniscus. These three curves meet at a junction point c. As the various dynamic phenomena that occur when a floating bubble bursts depend largely on its initial shape, the accurate prediction of this shape is important [21–27]. If the thickness and drainage of the liquid film can be neglected, then the shape of the bubble in the quasi-equilibrium state is determined by

the Young–Laplace equation representing the balance between the forces of hydrostatic pressure and capillary action [28–32]. Floating bubbles vary in shape from spherical to hemispherical, depending on their size. Therefore, the Bond number, *Bo*, is used as a key parameter.
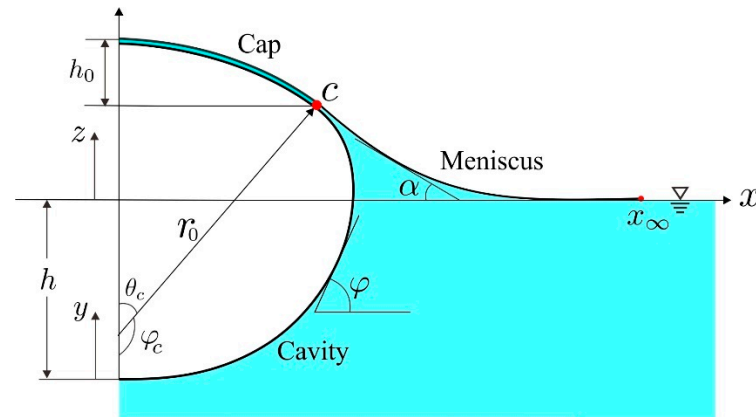

Figure 1. The schematic configuration of a floating bubble.

Bashforth and Adams [28] presented a systematic theoretical equation for hydrostatic pressure and capillary forces and obtained a series solution of drops of fluids. Subsequently, Toba [29] calculated the shapes of floating bubbles by using a semi-graphical method. At the same time, Princen [30] used the Table of Bashforth and Adams [28] to find the junction point and calculate the shapes of bubbles of various sizes. Medrow and Chao [31] numerically calculated the bubble shape for a broader range of the bubble sizes (which corresponds to a range of $0.003 < Bo < 241$, computed based on the parameter B values of [31]), and derived an analytic solution using a perturbation technique for tiny bubbles that are difficult to calculate numerically. Recently, Lhuissier and Villermaux [23] obtained the bubble shape via a method similar to that of Toba [29]; however, there is no detailed information on their numerical method and on the accuracy of their solution. Bartlett [32] used a similar method to Princen [30] and presented the shapes of bubbles for Bond numbers between 0.1 to 100. Cohen et al. [33] developed a model considering the film weight of giant soap bubbles and compared the results of numerical solutions and experiments. Shaw and Deike [34] studied the coalescence of floating bubbles for a wide range of Bond number, and characterized the evolution of the underwater neck and the surface bridge. Miguet et al. [35] investigated the life of a floating bubble by exploring the role of drainage and evaporation on film thinning. Despite a long period of study, the bubble sizes used for analysis have been limited, and there is no rigorous evaluation of the accuracy and robustness of the numerical methods used.

As bubble shape parameters play an important role in the theory describing various dynamic phenomena related to floating bubbles [36], accurate prediction of the bubble parameter is crucial, especially in a wide range of Bond numbers. For instance, the lifetimes of floating bubbles are related to the surface area of the bubble film [15]. The jet velocity generated when the bubble bursts is related to the depth of the cavity, and the amount of aerosol emitted depends on the radius and height of the cap [23,27]. Koch et al. [5] used the correlation between the dimensionless cap area and the dimensionless diameter to calculate the number of film droplets generated in the bubble bursting process, and the correlation between the dimensionless base radius and the dimensionless diameter to obtain the critical film thickness. Teixeira et al. [37] employed a perturbation method for large bubbles to obtain analytical expressions for bubble parameters as a function of the Bond number, and compared their results with experimental data. Puthenveettil et al. [36] also derived approximate analytical solutions for bubble parameters over a moderate range of Bond number ($0 < Bo < 1$) and compared these with their experimental results. Moreover, to the best of the present author's knowledge, no study has yet been published detailing the

correlations between the Bond number and various bubble parameters over an extensive range of Bond numbers.

In the present work, an improved numerical procedure is proposed to calculate the shapes of floating bubbles over a much wider range of Bond numbers than that examined in the previous studies. The proposed method is validated against the earlier numerical and experimental results to prove its accuracy and robustness. New correlations between the Bond number and several important bubble parameters, along with their asymptotic relations, are then provided.

The novelty of this study is as follows. A new method is developed by introducing specific functions for accurately finding the location of the connection points on the bubble surface regardless of the ODE solvers and their boundary points. An improved algorithm to find the junction point is developed, based on a novel function to determine the type of meniscus.

2. Theoretical Model

A slightly modified form of the theoretical model presented by Toba [29] and Medrow and Chao [31] is used in the present work. Thus, the shape of the floating bubble is described by the Young–Laplace equation:

$$\Delta p = \sigma \left(\frac{1}{r_1} + \frac{1}{r_2} \right), \tag{1}$$

where Δp is the pressure difference across the interface, σ is the surface tension, and r_1 and r_2 are the principal radii of curvature.

A half-section of an axisymmetric bubble floating on a liquid is presented, along with its associated parameters, in Figure 1, where $h > 0$ is the depth of the cavity below the undisturbed liquid surface, x_∞ is the point where the meniscus meets the undisturbed surface, and φ and α are the tangent angles of the cavity and meniscus curves, respectively.

If the thickness of the cap film is ignored, then the cap has a spherical shape with a radius r_0, and Equation (1) can be written as

$$\Delta p_0 = \frac{4\sigma}{r_0}, \tag{2}$$

where Δp_0 denotes the pressure difference across the cap film. Furthermore, if the weight of gas inside the bubble is neglected, then the cavity satisfies

$$\Delta p_0 + \rho g z = \sigma \left(\frac{1}{r_1} + \frac{1}{r_2} \right), \tag{3}$$

where ρ and g denote the liquid density and gravitational acceleration, respectively,

Similarly, the meniscus shape is given by

$$- \rho g z = \sigma \left(\frac{1}{r_1} + \frac{1}{r_2} \right). \tag{4}$$

As the bubble shape is a surface of revolution about the z-axis, the principal radii of curvature are given as

$$\frac{1}{r_1} = \frac{\sin \varphi}{x}, \tag{5}$$

$$\frac{1}{r_2} = \frac{d \sin \varphi}{dx}. \tag{6}$$

By using the capillary length, $a = \sqrt{2\sigma/\rho g}$, the bubble parameters are nondimensionalized as given by

$$x = aX, \ z = aZ, \ y = aY, \ h = aH, \ r_0 = aR_0. \tag{7}$$

Substituting Equations (2) and (5)–(7) into Equation (3) yields the dimensionless ordinary differential equations (ODEs) for the cavity shape, given here as

$$\frac{\mathrm{d}\sin\varphi}{\mathrm{d}X} = 2Y - \frac{\sin\varphi}{X} + B, \tag{8}$$

$$\frac{\mathrm{d}Y}{\mathrm{d}X} = \tan\varphi, \tag{9}$$

where the parameter B represents the dimensionless pressure difference across the bottom of the bubble, as defined by

$$B = \frac{4}{R_0} - 2H. \tag{10}$$

Equations (8) and (9) can be rewritten with an independent variable Y as

$$\frac{\mathrm{d}\cos\varphi}{\mathrm{d}Y} = -2Y + \frac{\sin\varphi}{X} - B, \tag{11}$$

$$\frac{\mathrm{d}X}{\mathrm{d}Y} = \cot\varphi. \tag{12}$$

Application of the L'Hospital's rule, i.e., $\lim_{\varphi\to 0}\sin\varphi/X = \lim_{\varphi\to 0}\mathrm{d}\sin\varphi/\mathrm{d}X$, then leads to the first initial condition of Equations (8) as follows:

$$\left.\frac{\mathrm{d}\sin\varphi}{\mathrm{d}X}\right|_{X=0} = \frac{B}{2}. \tag{13}$$

The second initial condition of Equation (9) is simply given as

$$\left.\frac{\mathrm{d}Y}{\mathrm{d}X}\right|_{X=0} = 0. \tag{14}$$

Similarly, the relation $\alpha = \pi - \varphi$ is used to obtain the ODEs for the meniscus shape as follows:

$$\frac{\mathrm{d}\sin\alpha}{\mathrm{d}X} = -2Y - \frac{\sin\alpha}{X} + 2H, \tag{15}$$

$$\frac{\mathrm{d}Y}{\mathrm{d}X} = -\tan\alpha. \tag{16}$$

The boundary conditions of Equations (15) and (16) at $X = X_\infty$ are given as

$$\sin\alpha_\infty = 0 \quad \text{and} \quad Y_\infty = 0 \tag{17}$$

At the junction point c, the geometrical relationship given in Equation (18) must be satisfied:

$$R_0 = \frac{X_c}{\sin\varphi_c}. \tag{18}$$

From Equations (10) and (18), the relation between H and B is given as

$$H = \frac{2\sin\varphi_c}{X_c} - \frac{B}{2}. \tag{19}$$

As the cap is spherical with a radius R_0, its shape is given by

$$X = R_0\sin\varphi, \tag{20}$$

$$Y = Y_c + R_0(\cos\varphi_c - \cos\varphi). \tag{21}$$

The volume of the bubble is computed analytically via integration by parts [38]. The volume of the cap is given by

$$V_{cap} = \pi H_0^2 \left(R_0 - \frac{H_0}{3} \right),\tag{22}$$

where $H_0 = R_0(1 + \cos \varphi_c)$.

The volume of the cavity is given by

$$V_{cavity} = \pi X_c^2 \left(Z_c + \frac{1}{R_0} \right).\tag{23}$$

The surface area of the cap is obtained as

$$A_{cap} = 2\pi R_0 H_0.\tag{24}$$

However, there is no analytic form for the surface area of the cavity. It should be numerically integrated as follows:

$$A_{cavity} = \int_0^{X_{45}} \frac{X}{\cos \varphi} dX + \int_{Y_{45}}^{Y_c} \frac{Y}{\sin \varphi} dY,\tag{25}$$

where X_{45} and Y_{45} respectively denote the X and Y positions on the cavity at $\varphi = \pi/4$.

The Bond number is defined by

$$Bo = \frac{\rho g r_e^2}{\sigma},\tag{26}$$

where r_e denotes the equivalent spherical radius of the bubble.

3. Numerical Procedure

Given the parameter B, the shape of the floating bubble can be determined. Since the bubble is symmetric about the z-axis, only half of it is needed. First, the shape of the cavity shape between the bottom and the junction point c is calculated, then the shape of the meniscus between the point c and the boundary point X_∞ is determined. Finally, the shape of the circular cap is quickly obtained. The junction point c between the cavity and the meniscus is not given analytically and should be found via a numerical iterative method. The accuracy of the bubble shape is significantly affected by the accuracy with which c is located.

The dimensionless height H is used to determine whether the guessed junction point $\widetilde{c}$ matches the exact point c. Given the position of $\widetilde{c}$, H is readily calculated from Equation (19). Furthermore, after computing the meniscus shape, another height, $\widetilde{H} = Y_\infty$, can be obtained. Thus, the bubble shape is considered to have converged when the error $\varepsilon_H = \left| H - \widetilde{H} \right|$ falls within a defined level of tolerance that indicates the accuracy of the numerical method used.

3.1. Improving the Accuracy of the Cavity Shape

The cavity shape can be obtained by integrating Equations (8) and (9) or Equations (11) and (12) numerically. However, previous studies have shown that it is necessary to divide the cavity into two [29,32,39] or three [31] parts in order to avoid divergence of Equations (8) and (9) at $\varphi = \pi/2$. In the present study, when the cavity was divided into two parts, the numerical error was found to increase rapidly as the bubble size decreased (see Figure 6). Hence, the cavity shape was divided into the following three parts or intervals: (I) $0 \leq \varphi < \pi/4$, (II) $\pi/4 \leq \varphi < 3\pi/4$, and (III) $3\pi/4 \leq \varphi < \pi$, and Equations (8) and (9) were applied to intervals (I) and (III), while Equations (11) and (12) were applied to interval (II). However, because φ is not an independent variable in these equations, the numerical integrations are not completely finished at $\varphi = \pi/4$ and $\varphi = 3\pi/4$. Hence, a conventional method is to set an arbitrary far point X_f (or Y_f) as a boundary condition of the ODEs and

to finish the calculation when φ is just greater than $\pi/4$ (or $3\pi/4$). Unfortunately, this leads to potential errors at the endpoint X_{45} (or Y_{135}) of the divided cavity depending on ODE solvers. The conventional method works well on medium-sized bubbles, but produces a severe error in large bubbles, especially at the position of X_{45}, because the bottom of the cavity becomes substantially flat. This error is not only affected by the boundary points X_f (or Y_f), but also by the tolerance of the ODE solver.

To remedy this problem, an improved method was proposed for accurately finding the location of the connection points X_{45} and Y_{135} regardless of the ODE solvers and their boundary points. In this approach, a monotonically increasing function $f(x; \phi)$ is defined as follows:

---

function $f(x; \phi)$
        Integrate Equations (8) and (9) from $X = 0$ to x to find $\sin \varphi$ at the endpoint
        return $(\sin \phi - \sin \varphi)$
end function

An accurate position $x = X_{45}$ is then found by solving $f(x; \pi/4) = 0$ in the interval $0 < x < X_f$ using a root-finding technique. Here, the boundary point X_f is any value greater than X_{45}; usually, $X_f \approx 100$ is appropriate for most of the bubble sizes considered in this study. As shown in Figure 2b, X_f does not affect the accuracy of the solution obtained using this method at all. Once X_{45} has been determined, Equations (8) and (9) are integrated again from $X = 0$ to X_{45} to obtain the first part of the cavity profile along with the remaining Y_{45} and φ_{45}. Similarly, the second part of the cavity and its endpoint $(X_{135}, Y_{135}, \varphi_{135})$ can be computed using the following function:

---

function $g(y; \phi)$
        Integrate Equations (11) and (12) from $Y = Y_{45}$ to y to find $\cos \varphi$ at the endpoint
        return $(\cos \phi - \cos \varphi)$
end function

(a)   (b)
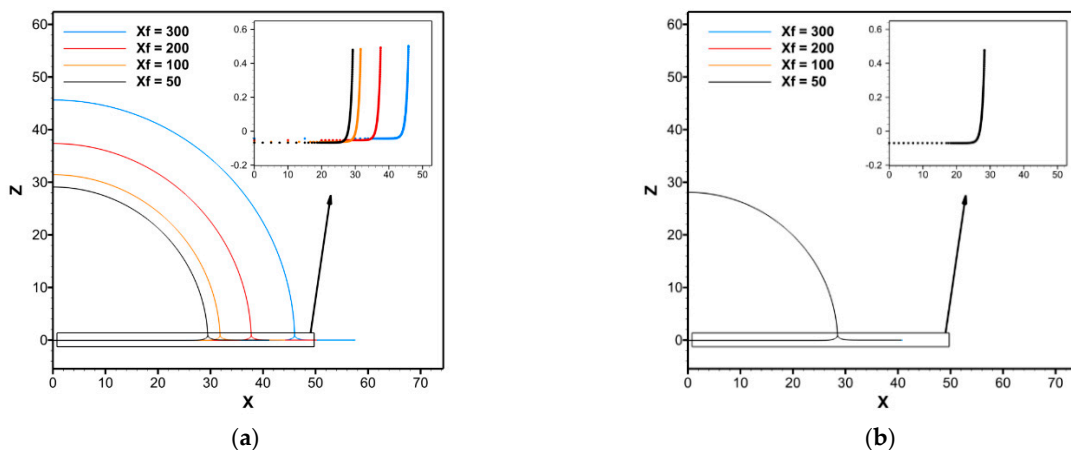
Figure 2. Comparison of the bubble shapes obtained according to the boundary point X_f of Equations (8) and (9) for a large bubble ($B = 10^{-16}$) using (**a**) the conventional method, and (**b**) the improved method involving the root-finding technique. The tolerance of the ODE solver is set to 10^{-9}. The insets plot the cavity profiles up to 45 degrees and are not scaled.

The computed bubble shapes according to the position of the boundary point X_f for a large bubble ($B = 10^{-16}$) are presented in Figure 2. Here, the bubble shapes are seen to vary significantly depending on X_f when the conventional technique is used (Figure 2a). When the root-finding method is used, however, the bubble shapes not affected by X_f (Figure 2b).

Similarly, the effect of ODE solver tolerances for the same size of bubble are presented in Figure 3. Here, the bubble shape changes slightly according to the tolerance using the

improved method (Figure 3b), but the results obtained using the conventional method are unacceptable (Figure 3a). Therefore, it is essential to compute the connection point accurately for large bubbles.

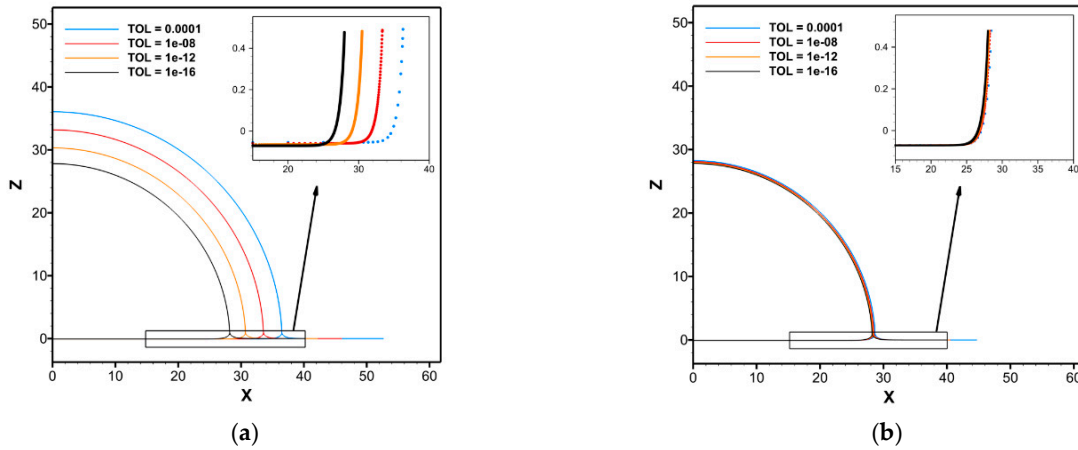**Figure 3.** Comparison of the bubble shapes obtained according to the tolerance of the ODE solver for a large bubble ($B = 10^{-16}$) using (**a**) the conventional method, and (**b**) the improved method involving the root-finding technique. The insets plot the cavity profiles up to 45 degrees and are not scaled.

3.2. Finding the Junction Point Based on the Type of Meniscus

There are two general approaches to finding the junction point c according to the direction of integration of the meniscus. The first approach is to integrate the meniscus from $X = X_\infty$ to X_c in the negative X-direction [29,31]. Here, X_∞ is sought in an iterative manner so that the derivatives of the meniscus and cavity profiles match at the junction point c. However, it is difficult to compute the shape of the meniscus using this method because the initial slope becomes zero when the exact initial condition, $Z_\infty = \alpha_\infty = 0$ at $X = X_\infty$, is applied. To circumvent this, Toba [29] and Freud and Freud [40] employed $Z_a = \alpha_a = 0.00001$ at $X = X_a < X_\infty$ as an initial condition. Medrow and Chao [31] further improved this method by using an approximate analytical solution of Z_a with the Bessel function. Nevertheless, as these methods do not give an exact initial condition at $X = X_\infty$, the accuracy of the solution is still limited.

The second approach is to integrate the meniscus from X_c to X_∞ in the positive X-direction [23,30,32]. Although this approach has the advantage of obtaining the X_∞ position more precisely, there is another difficulty in that the meniscus shape changes dramatically around the junction point c, as shown in Figure 4.
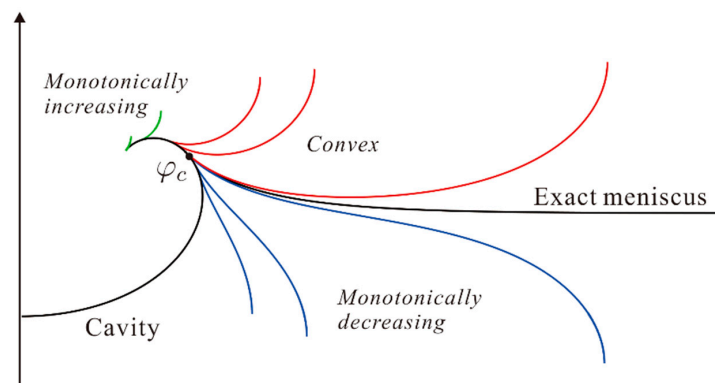

Figure 4. Three types of the meniscus shape according to the location of the guessed junction point. Here, φ_c is the angle at the exact junction point.

Hence, a method for effectively locating the junction point c is proposed herein by using a specific function that distinguishes the type of meniscus shape. A conventional bisection method for finding c narrows the interval by comparing the sign of $H - \widetilde{H}$ at both ends of the solution interval. At each iteration step, it is necessary to find the height $\widetilde{H}$, which is calculated differently depending on the meniscus type: if the meniscus profile is convex, its minimum value is chosen; if the meniscus profile is monotonically decreasing, an inflection point is selected. Interestingly, without calculating $\widetilde{H}$, the bisection method can become simpler by considering the meniscus type only. Hence, the following function is defined to determine whether a meniscus is convex at a guessed junction point:

---

function is_meniscus_convex(c)

         Integrate Equations (15) and (16) from $X = X_c$ to X_{max} to find $\sin \alpha_{max}$,
             where $X_{max} > X_\infty$ is any large value
           return the logical value of $(\sin \alpha_c \cdot \sin \alpha_{max} < 0)$

end function

This function is then used to modify the bisection method as Algorithm 1:

Algorithm 1 Modified bisection method

Input: P_L, P_R
Output: P_c
for $n = 1$ **to** n_{max}
     $P_c = (P_L + P_R)/2$
     if is_meniscus_convex(P_c)
         $P_R = P_c$
     else
         $P_L = P_c$
     end if
end for

---

where P represents the X or Y value on the cavity. The maximum number of iterations is given by $n_{max} = \log_2 \left(|P_L^0 - P_R^0| / \epsilon \right)$. Here, ϵ and $\left[P_L^0, P_R^0 \right]$ are the error tolerance and initial interval of the bisection method, respectively. If φ_c is between $90°$ and $135°$, the initial interval is $[Y_{90}, Y_{135}]$; if φ_c is between $135°$ and $180°$, the initial interval is $[X_{135}, X_{180}]$, where $X_{180} \neq 0$. However, if Y_{90} and X_{180} are not sufficiently accurate, this method may fail to find the junction point c in the case of very small or large bubbles. The exact positions of Y_{90} and X_{180} can be obtained by solving the equations $g(y; \pi/2) = 0$ and $f(x; \pi) = 0$, respectively. Once the junction point c is obtained, X_∞ can be found by using the following function $q(x)$, and then the meniscus shape:

---

function $q(x)$

         Integrate Equations (15) and (16) from $X = X_c$ to x to find $\sin \alpha$ at the endpoint
           return $\sin \alpha$

end function

This modified bisection method is more efficient and robust than the conventional one because there are no expensive routines to find the minimum or inflection point of the meniscus. Although a similar meniscus type to that used herein was previously used by Princen [30], the method employed therein remained limited in terms of bubble size and accuracy because it relied on Bashforth and Adam's table [28].

The overall procedure for calculating a floating bubble shape is summarized in Algorithm 2.

Algorithm 2 The improved numerical procedure for calculating the shape of a floating bubble

---

Input: *B*

Output: *Floating bubble shape and parameters*

Calculate the first part of the cavity profile C_1 by integrating Equations (8) and (9) from $\varphi = 0$ to $\pi/4$ and by solving $f(x; \pi/4) = 0$.

Calculate a part of the cavity profile C_2' by integrating Equations (11) and (12) from $\varphi = \pi/4$ to $3\pi/4$ and by solving $g(y; 3\pi/4) = 0$.

if is_meniscus_convex(P_{135})

    Find Y_{90} by solving $g(y; \pi/2) = 0$.

    Find the junction point Y_c by using the modified bisection method in $[Y_{90}, Y_{135}]$.

    Calculate the rest of the cavity profile C_2 by integrating Equations (11) and (12) from $Y = Y_{45}$ to Y_c.

else

    Find X_{180} by solving $f(x; \pi) = 0$.

    Find the junction point X_c by using the modified bisection method in $[X_{135}, X_{180}]$.

    Calculate a part of the cavity profile C_3 by integrating Equations (8) and (9) from $X = X_{135}$ to X_c.

Set the rest of the cavity profile as $C_2 = C_2' \cup C_3$.

end if

Calculate the meniscus profile C_m by integrating Equations (15) and (16) from $\alpha = \alpha_c$ to α_∞.

Calculate the cap profile C_0 by computing Equations (20) and (21) from $\varphi = \varphi_c$ to π.

Combine the profiles to obtain the floating bubble shape: $C = C_1 \cup C_2 \cup C_m \cup C_0$.

---

4. Results and Discussion

In the present study, the ODE solver employs a variable step, the 4th and 5th-order Runge–Kutta algorithm using Dormand and Prince pairs [41]. A range of the Bond numbers, i.e., $5 \times 10^{-5} < Bo < 5000$, is applied to the improved numerical method. Accordingly, the results obtained using the conventional and improved methods are compared in the following subsection. Then the present results are compared with those of previous computational and experimental studies.

4.1. Comparison between the Conventional and Improved Methods

The conventional and improved methods are compared for large bubbles in Figure 5. Here, it can be seen that a smaller value of *B* corresponds to a larger bubble size (Figure 5a). Thus, when $B = 1 \times 10^{-7}$, the bubble shapes obtained using the two different methods are almost identical. However, when $B = 1 \times 10^{-14}$, there is a slight difference between the two results, and when $B = 1 \times 10^{-22}$, the two methods show a significant discrepancy in the obtained bubble shapes. The cause of inaccuracy in the conventional method is demonstrated in Figure 5b, where the dimensionless cap radius R_0 is seen to increase abnormally as the parameter *B* decreases in the conventional method.

The conventional and improved methods are compared for small bubbles in Figure 6. Here, when $B = 1000$, the bubble shapes obtained using both methods are almost identical (Figure 6a). However, when $B = 2000$ and 3000, the conventional method raises the bubble in a non-physical manner because the bisection method does not converge and gives a negative value of *H*. As shown in Figure 6b, when *B* is small, the dimensionless absolute height $|H|$ is the same in both methods; however, as *B* becomes larger, $|H|$ fluctuates significantly in the conventional method. These results clearly demonstrate that the improved method should be used to calculate large or small bubbles robustly.
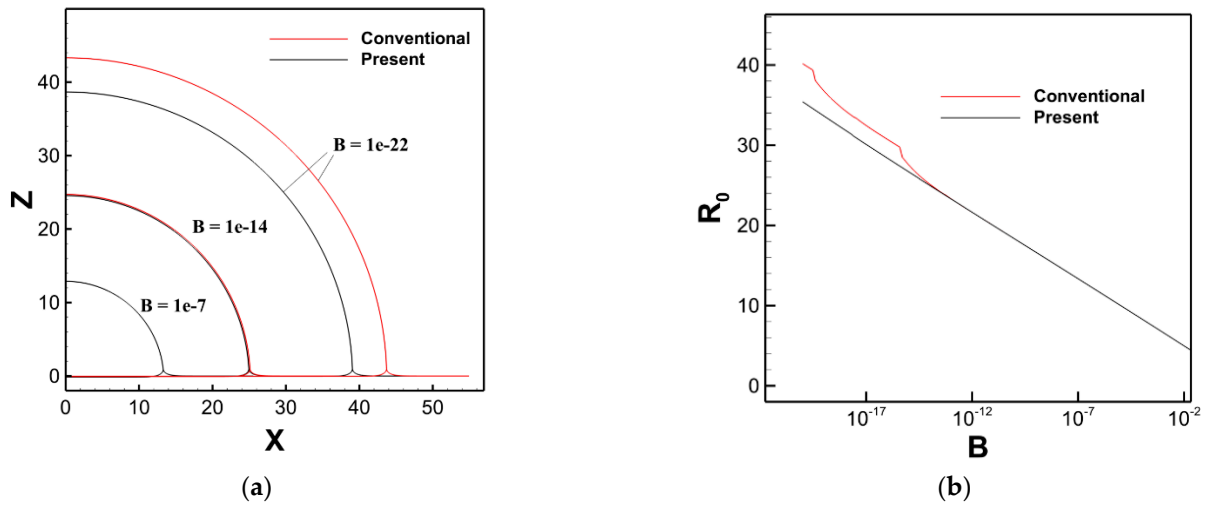
(**a**)

(**b**)

Figure 5. Comparison of the conventional (red) and the improved (black) methods for large bubbles. The tolerance of the ODE solver is set to 10^{-12}. (**a**) Floating bubble shapes for the following three large bubble sizes: $B = 1 \times 10^{-7}, 1 \times 10^{-14}$, and 1×10^{-22}. (**b**) The dimensionless cap radius R_0 is plotted with respect to the parameter B.

(**a**)

(**b**)
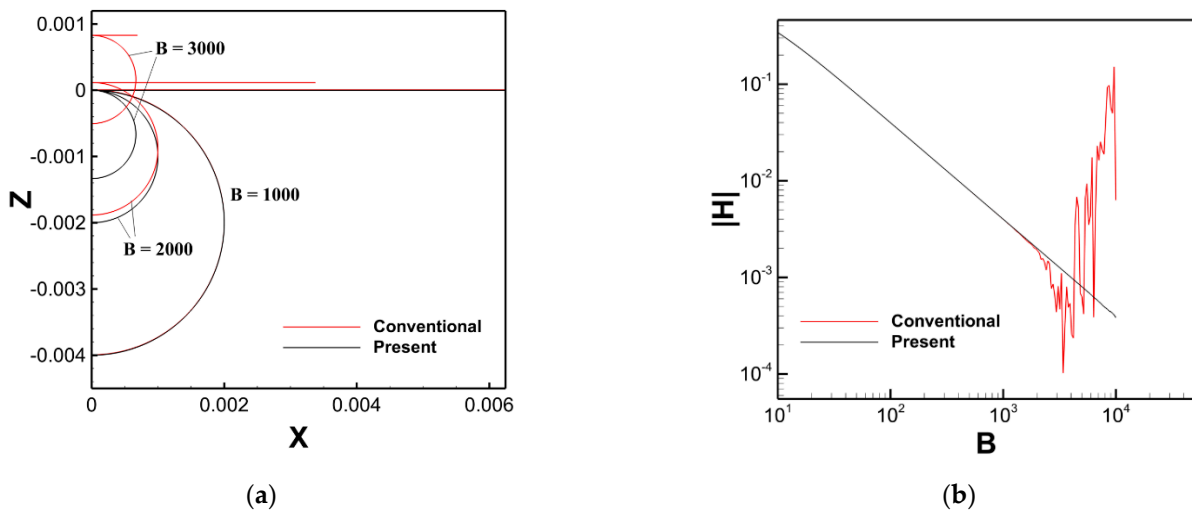
Figure 6. Comparison of the conventional (red) and the improved (black) methods for small bubbles. The tolerance of the ODE solver is set to 10^{-12}. (**a**) Floating bubble shapes for the following three small bubble sizes: $B = 1000, 2000$, and 3000. (**b**) The dimensionless absolute height $|H|$ is plotted with respect to the parameter B.

4.2. Comparison of the Present Results with the Earlier Numerical and Experimental Results

The present computational results are compared with the previously published numerical results in Table 1. Various bubble parameters were previously calculated in the range of B = 1–20, B = 0.28–8, and $B = 4 \times 10^{-8}$–50 by Toba [29], Princen [30], and Medrow and Chao [31], respectively. However, Princen [30] used the parameter β in place of B, where the relationship between these is given by

$$B = \sqrt{8/\beta} \quad \text{and} \quad X = (x/b)\sqrt{\beta/2}, \tag{27}$$

where X denotes the dimensionless parameter of the present work, and (x/b) denotes the dimensionless parameters of Princen's work. The computed parameters in Table 1 agree well with one another, with the exception of Toba's parameters. This is because Toba employed a semi-graphical technique of limited accuracy. The earlier methods used an approximate analytical solution for tiny bubbles [31] or an interpolation method with a

pre-calculated Table [30], so the sizes considered were narrow. Medrow and Chao [31] used the boundary conditions of $Z_a = 0.00001$ and $\sin \alpha_\infty \leq 0.0001$. Princen [30] searched the junction point until both ΔX_c and ΔZ_c were less than $\varepsilon = 0.5 \times 10^{-5}$. In contrast, the present calculations maintain an accuracy of $|\sin \alpha_\infty| < 5 \times 10^{-20}$ and $\varepsilon_H < 5 \times 10^{-8}$, thus providing much more precise results.

Table 1. Comparison of the present numerical results with those of Toba [29], Princen [30], and Medrow and Chao [31] for the selected bubble parameters.

B	Authors	X_c	Y_c	φ_c	R_0	V	H
50	Medrow	0.0026045	0.07970	178.13	0.07975	0.0002672	0.07921
	Present	0.002604455	0.07958193	178.1285	0.07974769	0.000267229	0.07909536
20	Toba	0.016	0.194	175.3	0.196	0.0041	0.184
	Medrow	0.016011	0.19481	175.32	0.1963	0.004108	0.1897
	Present	0.01601056	0.1947944	175.3211	0.1962769	0.004107305	0.1896872
8	Princen	0.09101	0.44341	168.443	0.45428	0.05846	-
	Present	0.09100837	0.4434090	168.4433	0.4542754	0.05846040	0.4026157
7	Toba	0.117	0.493	166.5	0.502	0.0863	0.433
	Medrow	0.11520	0.49307	166.88	0.5076	0.08463	0.4401
	Present	0.1152068	0.4930890	166.8816	0.5075995	0.08463203	0.4401145
4	Toba	0.284	0.722	158.4	0.772	0.3680	0.592
	Princen	0.28217	0.72309	158.574	0.77245	0.36408	-
	Medrow	0.28217	0.72310	158.57	0.7724	0.3641	0.5892
	Present	0.2821735	0.7230909	158.5740	0.7724442	0.3640805	0.5891839
2	Toba	0.655	0.989	145.9	1.169	1.67	0.711
	Princen	0.65599	0.98789	146.014	1.17354	1.67520	-
	Medrow	0.65598	0.98782	146.02	1.174	1.675	0.7042
	Present	0.6559949	0.9878898	146.0140	1.173535	1.675189	0.7042526
1	Toba	1.159	1.161	134.2	1.621	5.51	0.734
	Medrow	1.1603	1.15854	134.56	1.629	5.505	0.7281
	Present	1.160338	1.158526	134.5617	1.628556	5.505488	0.7280821
0.5	Princen	1.71400	1.23904	125.860	2.11488	13.7728	-
	Medrow	1.7140	1.23890	125.87	2.115	13.77	0.6956
	Present	1.714005	1.239067	125.8599	2.114874	13.77346	0.6956826
0.4	Princen	1.89485	1.25155	123.611	2.27520	17.6919	-
	Medrow	1.8948	1.25152	123.61	2.275	17.69	0.6790
	Present	1.894856	1.251574	123.6100	2.275215	17.69363	0.6790378
0.001	Medrow	6.5244	1.14954	101.91	6.668	565.2	0.2994
	Present	6.524375	1.149610	101.9076	6.667858	565.2013	0.2994464
4×10^{-8}	Medrow	13.947	1.07121	95.66	14.02	5527	0.1427
	Present	13.94652	1.071357	95.6803	14.01534	5523.744	0.1427007

　　　The experimental results of Teixeira et al. [37] are compared with the present numerical results for selected bubble parameters in Figure 7a, where the parameters are plotted with respect to the Bond number based on the cap radius, i.e., $Bo_0 = \rho g r_0^2 / \sigma$. Here, the present computations are seen to agree well with the experimental results, except for the H^* values. For this parameter, the numerical results obtained using Surface Evolver S/W [42] have shown a similar trend to the present computations, as described in [37]. Meanwhile, the experimental results of Puthenveettil et al. [36] are compared with the present numerical results for selected parameters in Figure 7b, where Z_m denotes the height of the bubble top above the undisturbed surface. All parameters are normalized with respect to the equivalent bubble radius R_e. The experimental results agree well with the present computation, except that the present computation overestimates the experimental data for R_0 / R_e. Notably, the numerical results of Puthenveettil et al. [36] also overestimate R_0 / R_e by a similar amount.
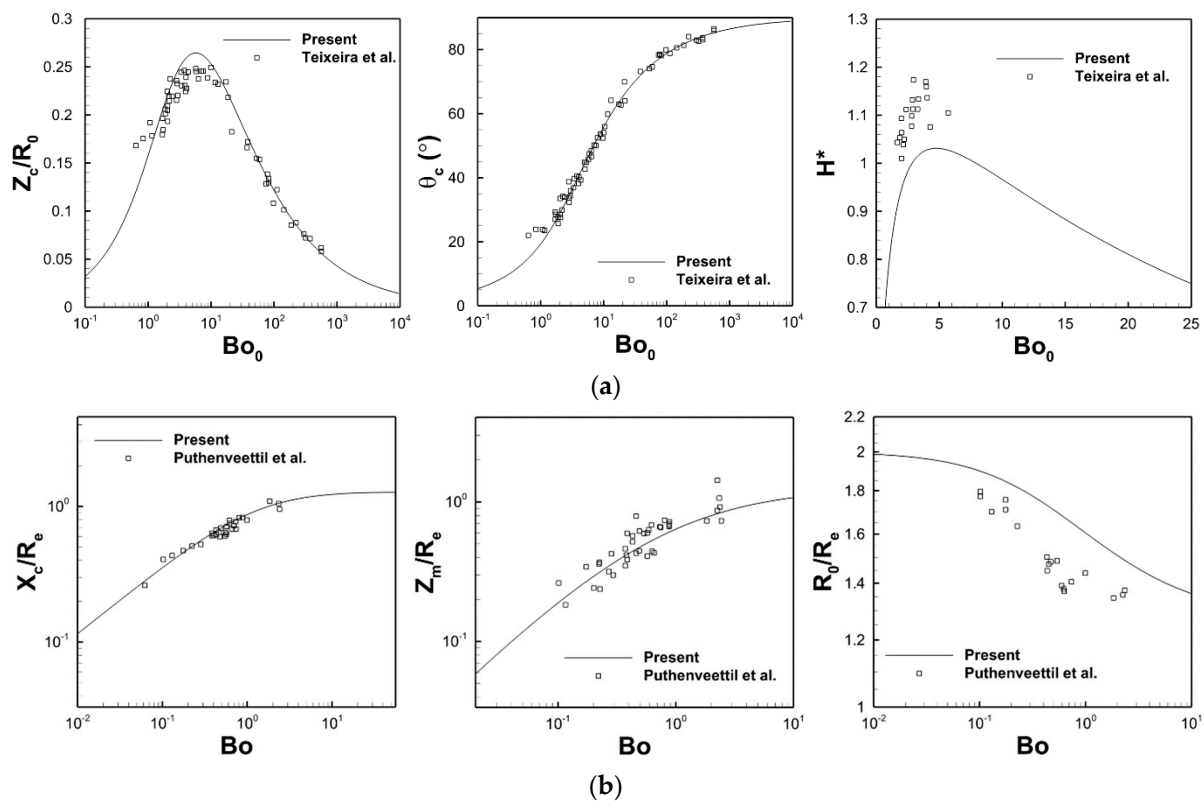
Figure 7. Comparison of the present numerical results with the experimental results of (**a**) Teixeira et al. [37] and (**b**) Puthenveettil et al. [36] for selected bubble parameters, where $H^* = \sqrt{2H}$.

The presently computed profiles for bubbles of various sizes (red outlines) are compared with the experimental photographs obtained by Teixeira et al. [37] and Puthenveettil et al. [36] in Figure 8. In addition, the present predictions for the angle of the junction point (θ_c) are compared with those measured by Teixeira et al. [37] in Table 2. Teixeira et al. [37] used a soap solution ($\sigma = 0.0282$ N/m), and the images were taken in the range of $X_c = 1$ to 32.5 mm (Figure 8a). Here, the calculated bubble shapes are seen to match the experimental images well, although the results in Table 2 indicate slightly different values for the angle of the junction point (θ_c). Specifically, the present computational work predicts θ_c to be about $1 - 2$ degrees higher than that measured by Teixeira et al. [37] Meanwhile, the experimental investigations of Puthenveettil et al. [36] were performed on various liquids (e.g., water and ethanol), and the photographs were taken for $Bo = 0.004$ to 2.46 (Figure 8b). However, when the Bond numbers measured by Puthenveettil et al. [36] were used in the present computations, the resulting numerical profiles for large bubbles were quite different from the experimental photographs. Hence, the Bo values used in the present work were adjusted in order to provide a better match between the predicted and measured profiles. These adjusted Bond numbers are compared with those measured from Figure 8b in Table 3. Here, similar Bond numbers are predicted and measured for the two tiny bubbles, but the present computations predict much higher Bond numbers than those measured for the two large bubbles. While Teixeira et al. [37] measured the bubble cap radius and the junction angles to obtain an alternative form of Bond number (Bo_0), Puthenveettil et al. [36] calculated Bo by measuring the volume of a bubble from the experimental image. It is expected that obtaining Bo is more complicated than obtaining Bo_0 because the lower part of the floating bubble is immersed in the liquid, whereas the upper part is not. Therefore, the discrepancy in Table 3 is thought to be due to experimental errors or the limitations of the current theoretical model.
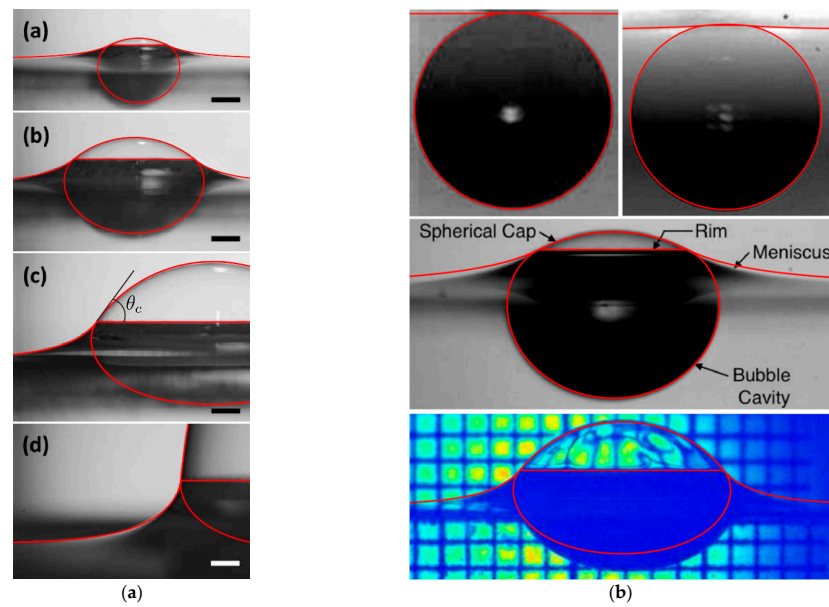
Figure 8. Comparison of the presently computed bubble profiles (red outlines) with the experimental photographs obtained by (**a**) Reprinted with permission from [37]. Copyright 2015 American Chemical Society (from top to bottom X_c = (a) 1, (b) 2.1, (c) 4.2 and (d) 32.5 mm) and (**b**) Reprinted from [36], with the permission of AIP Publishing.

Table 2. The angle of the junction point (θ_c) as measured experimentally by Teixeira et al. [37] and as predicted in the present work.

Image in Figure 8a	θ_c	
	Teixeira et al. [37]	**Present**
(a)	25.7	26.6
(b)	38.5	39.6
(c)	52.5	54.7
(d)	83.9	84.2

Table 3. The Bond numbers (B_O) measured by Puthenveettil et al. [36] and those of the present computational work.

Image in Figure 8b	*Bo*	
	Puthenveettil et al. [36]	**Present**
Top Left	0.004	0.004
Top Right	0.03	0.03
Middle	0.5	0.63
Bottom	2.46	3.5

4.3. Important Bubble Parameters and Profiles for a Wide Range of the Bond Numbers

The present numerical results for important bubble parameters in a wide range of Bond numbers ($10^{-40} < B < 1000$, corresponding to $8 \times 10^{-6} < Bo < 5723$) are listed in Table 4. The relative tolerance of the ODE solver is set to $TOL = 2.22 \times 10^{-16}$. For the range of B considered here, the present computations satisfy $|\sin \alpha_\infty| < 10^{-19}$ and $\varepsilon_H < 7 \times 10^{-8}$. Thus, the present method computes the boundary condition of the meniscus more accurately and converges the position of the junction point more precisely than the earlier methods. As a result, the present method provides highly precise and robust numerical results for a wide range of bubble sizes.

Table 4. The present numerical results for important bubble parameters.

B	Bo	X_c	Z_c	φ_c	H	H_0	R_0
1000	7.999957×10^{-6}	6.531920×10^{-6}	1.426955×10^{-7}	179.9064	0.003999773	5.333294×10^{-9}	0.003999968
500	3.199932×10^{-5}	2.612705×10^{-5}	8.835825×10^{-7}	179.8129	0.007998500	4.266541×10^{-8}	0.007999744
300	8.888362×10^{-5}	7.257102×10^{-5}	3.674190×10^{-6}	179.6881	0.01332701	1.975148×10^{-7}	0.01333215
200	0.0001999733	0.0001632667	1.131729×10^{-5}	179.5322	0.01998027	6.665443×10^{-7}	0.01999600
150	0.0003554713	0.0002902067	2.500423×10^{-5}	179.3762	0.02662265	1.579731×10^{-6}	0.02665720
100	0.0007995738	0.0006526751	7.571394×10^{-5}	179.0643	0.03986447	5.329410×10^{-6}	0.03996813
80	0.001248960	0.001019346	0.0001385365	178.8304	0.04974934	1.040468×10^{-5}	0.04993789
60	0.002218939	0.001810413	0.0002997670	178.4404	0.06611566	2.464071×10^{-5}	0.06652007
30	0.008836790	0.007193843	0.001842383	176.8804	0.1297692	0.0001958917	0.1321897
20	0.01973977	0.01601056	0.005107188	175.3211	0.1896872	0.0006540912	0.1962769
16	0.03062309	0.02474611	0.008773140	174.1542	0.2317490	0.001263504	0.2429617
10	0.07610977	0.06055737	0.02561974	170.6915	0.3420357	0.004930032	0.3743891
7	0.1483636	0.1152068	0.05297453	166.8816	0.4401145	0.01324675	0.5075995
4	0.3924363	0.2821735	0.1339070	158.5740	0.5891839	0.05338361	0.7724442
2	1.085626	0.6559949	0.2836372	146.0140	0.7042526	0.2004702	1.173535
1	2.399762	1.160338	0.4304443	134.5617	0.7280821	0.4858354	1.628556
0.5	4.422484	1.714005	0.5433848	125.8599	0.6956826	0.8759713	2.114874
0.2	8.186136	2.454823	0.6454278	117.9642	0.6195963	1.476051	2.779336
0.1	11.82990	3.007428	0.6984155	113.8375	0.5582908	1.959115	3.287901
0.03	19.73677	3.948336	0.7613356	108.9106	0.4642022	2.820973	4.173604
0.002	44.66426	6.005879	0.8378743	102.8796	0.3236288	4.787607	6.160882
2×10^{-5}	109.3486	9.416629	0.8949651	98.35707	0.2101250	8.134374	9.517693
4×10^{-8}	240.5064	13.94652	0.9286565	95.68030	0.1427007	12.62814	14.01534
3×10^{-12}	537.2599	20.80127	0.9520342	93.82031	0.09593434	19.45857	20.84759
2×10^{-18}	1197.575	30.99599	0.9677704	92.56740	0.06445970	29.63729	31.02714
1×10^{-25}	2310.565	42.99781	0.9767552	91.85180	0.04648970	41.63011	43.02028
1×10^{-40}	5723.091	67.57905	0.9852057	91.17865	0.02958871	66.20297	67.59335

B	X_{90}	X_h	V	A	X_∞	$\sin\alpha_\infty$	ε_H
1000	0.001999997	2.592758×10^{-5}	3.351005×10^{-8}	5.026523×10^{-5}	0.6035815	$-1.525375 \times 10^{-22}$	2.676590×10^{-8}
500	0.003999979	9.281963×10^{-5}	2.680740×10^{-7}	0.0002010577	1.730274	$-7.698510 \times 10^{-22}$	1.453944×10^{-8}
300	0.006666568	0.0002463152	1.241013×10^{-6}	0.0005584724	2.985969	$-3.153570 \times 10^{-22}$	7.827400×10^{-9}
200	0.009999667	0.0005332463	4.187953×10^{-6}	0.001256470	3.535465	$-1.123335 \times 10^{-21}$	1.095687×10^{-8}
150	0.01333254	0.0009204409	9.925456×10^{-6}	0.002233493	5.149609	$-2.827164 \times 10^{-22}$	2.132361×10^{-9}
100	0.01999733	0.001979302	3.348354×10^{-5}	0.005023872	6.959408	$-2.696805 \times 10^{-23}$	4.713860×10^{-10}
80	0.02499480	0.003009708	6.536818×10^{-5}	0.007847453	6.050189	$-3.036618 \times 10^{-22}$	3.593450×10^{-9}

Table 4. *Cont.*

60	0.03332100	0.005150905	0.0001547967	0.01394203	6.122253	$-3.366391 \times 10^{-22}$	7.635189×10^{-9}
30	0.06656836	0.01842589	0.001230227	0.05552427	7.955407	$-1.988549 \times 10^{-22}$	3.939505×10^{-9}
20	0.09967012	0.03801315	0.004107305	0.1240385	8.408457	$-4.855708 \times 10^{-23}$	6.727939×10^{-9}
16	0.1243594	0.05600981	0.007936283	0.1924426	9.236173	$-1.191350 \times 10^{-21}$	3.836083×10^{-9}
10	0.1974393	0.1218416	0.03109598	0.4785621	9.861832	$-3.807630 \times 10^{-22}$	5.996772×10^{-9}
7	0.2785360	0.2086884	0.08463203	0.9340670	10.87842	$-2.663932 \times 10^{-22}$	3.687912×10^{-9}
4	0.4664155	0.4271852	0.3640805	2.483857	11.63113	$-6.332112 \times 10^{-23}$	5.348933×10^{-9}
2	0.8182227	0.8158624	1.675189	6.968744	12.57281	$-8.638849 \times 10^{-22}$	6.609880×10^{-9}
1	1.278940	1.265220	5.505488	15.69547	12.89420	$-3.031094 \times 10^{-21}$	1.564443×10^{-8}
0.5	1.796671	1.728766	13.77346	29.45927	13.99436	$-1.192995 \times 10^{-21}$	9.942357×10^{-9}
0.2	2.507679	2.341705	34.68663	55.64825	14.57138	$-6.057025 \times 10^{-21}$	1.638346×10^{-8}
0.1	3.046686	2.803791	60.25804	81.40699	15.50268	$-9.881551 \times 10^{-22}$	1.074786×10^{-8}
0.03	3.973631	3.606096	129.8547	138.0179	17.51656	$-8.436210 \times 10^{-22}$	2.649258×10^{-9}
0.002	6.017921	5.421926	442.0626	319.0965	18.42952	$-1.661529 \times 10^{-21}$	1.674617×10^{-8}
2×10^{-5}	9.421791	8.550337	1693.416	794.3151	21.75908	$-7.942353 \times 10^{-21}$	2.212266×10^{-8}
4×10^{-8}	13.94893	12.82268	5523.744	1764.149	25.96071	$-2.333522 \times 10^{-20}$	3.959115×10^{-8}
3×10^{-12}	20.80236	19.40908	18,442.52	3967.061	33.13493	$-5.203562 \times 10^{-21}$	2.737275×10^{-8}
2×10^{-18}	30.99649	29.33207	61,375.84	8881.418	43.50420	$-2.452283 \times 10^{-20}$	2.283753×10^{-8}
1×10^{-25}	42.99807	41.10880	164,482.9	17,177.59	54.76092	$-8.969384 \times 10^{-20}$	6.884084×10^{-8}
1×10^{-40}	67.57916	65.37684	641,194.2	42644.47	80.35356	$-1.015233 \times 10^{-20}$	1.705349×10^{-8}

The calculated bubble shapes for $10^{-40} < B < 1000$ are presented in Figure 9, where each shape is drawn at equal intervals on a log scale of B. In the interval of $B = 10^{-40}$ to 10^{-4}, the bubble exhibits an almost hemispherical shape, and the cavity is virtually flat (Figure 9a). However, in the interval $10^{-4} < B < 0.1$, the shape becomes less hemispherical as the bottom of the bubble continues to descend into the liquid (Figure 9b). In the interval $0.1 < B < 10$, the shape continues to change from hemispherical to that of a bisected rugby ball (Figure 9c). Interestingly, the depth H is found to increase to a maximum value and subsequently decrease within this interval. In the interval $10 < B < 100$, the bubbles have acquired a nearly spherical shape and are seen to protrude only slightly above the undisturbed liquid surface (Figure 9d). Finally, in the interval $100 < B < 1000$, the bubbles are almost spherical and are almost entirely submerged in the liquid (Figure 9e).
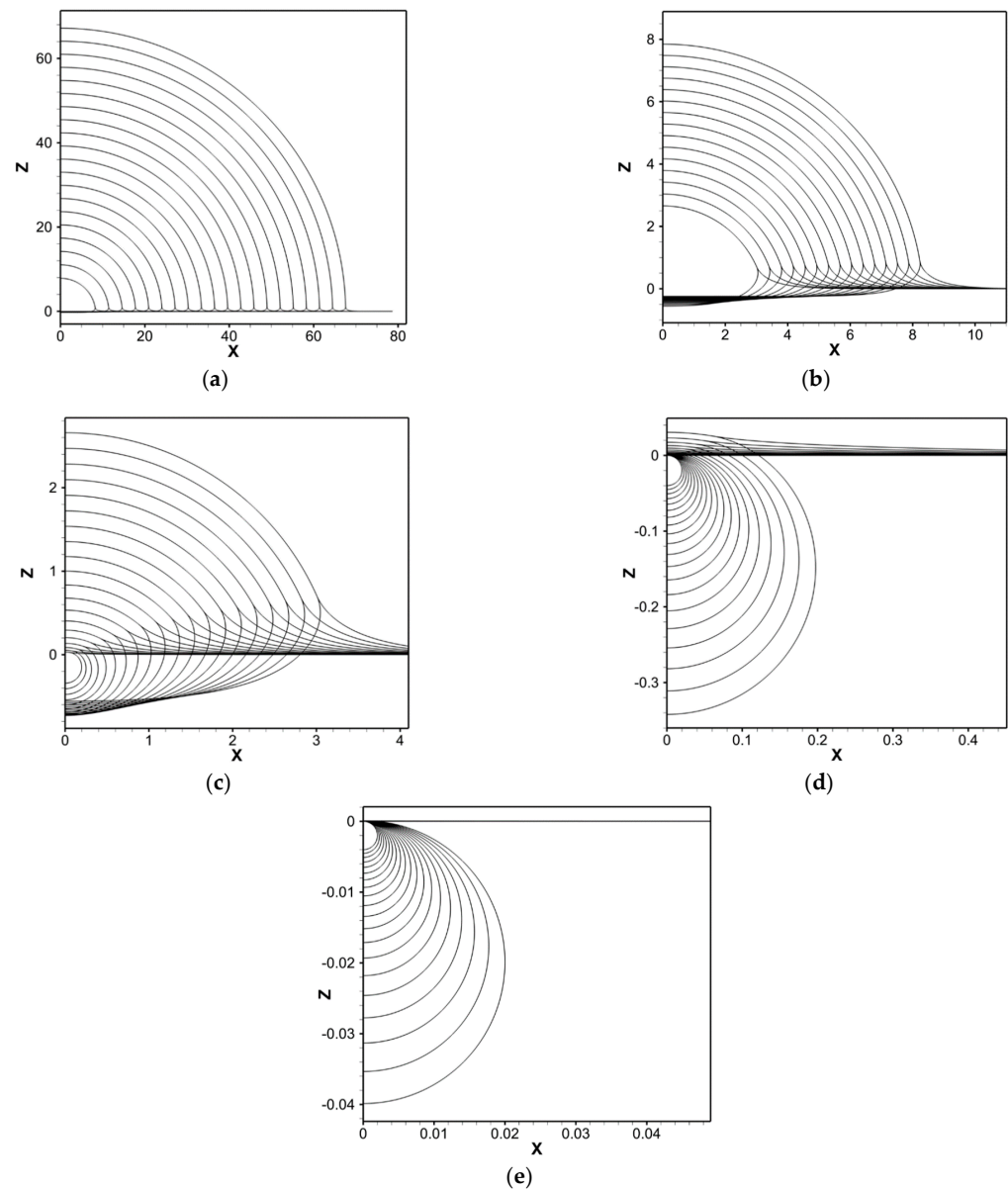
(a)

(b)

(c)

(d)

(e)

Figure 9. The computed bubble shapes for $10^{-4} < B < 1000$, where each shape is drawn at equal intervals on a log scale of B. (**a**) Twenty bubbles for $B = 10^{-40}$–10^{-4} ($Bo = 5723$–83.6). (**b**) Fifteen bubbles for $B = 10^{-4}$–0.1 ($Bo = 83.6$–11.8). (**c**) Twenty bubbles for $B = 0.1$–10 ($Bo = 11.8$–0.076). (**d**) Twenty bubbles for $B = 10$–100 ($Bo = 0.076$–8×10^{-4}). (**e**) Twenty bubbles for $B = 100$–1000 ($Bo = 8 \times 10^{-4}$–8×10^{-6}).

4.4. Correlations and Asymptotic Behaviors of the Bubble Parameters

The log–log plots of the various bubble parameters with respect to the Bond number for the interval of $5 \times 10^{-5} \leq Bo \leq 5000$ are presented in Figure 10. Each plot can be divided into the following three regions: (I) $5 \times 10^{-5} \leq Bo \leq 0.1$, (II) $0.1 \leq Bo \leq 100$, and (III) $100 \leq Bo \leq 5000$. The parameters for each interval are fitted with a fifth-order polynomial on the log-log scale according to Equation (28):

$$\log_{10} \Pi \approx \sum_{i=0}^{5} c_i \left(\log_{10} Bo\right)^i, \tag{28}$$

where Π denotes the dimensionless bubble parameters. The coefficients c_i are presented in Table 5.
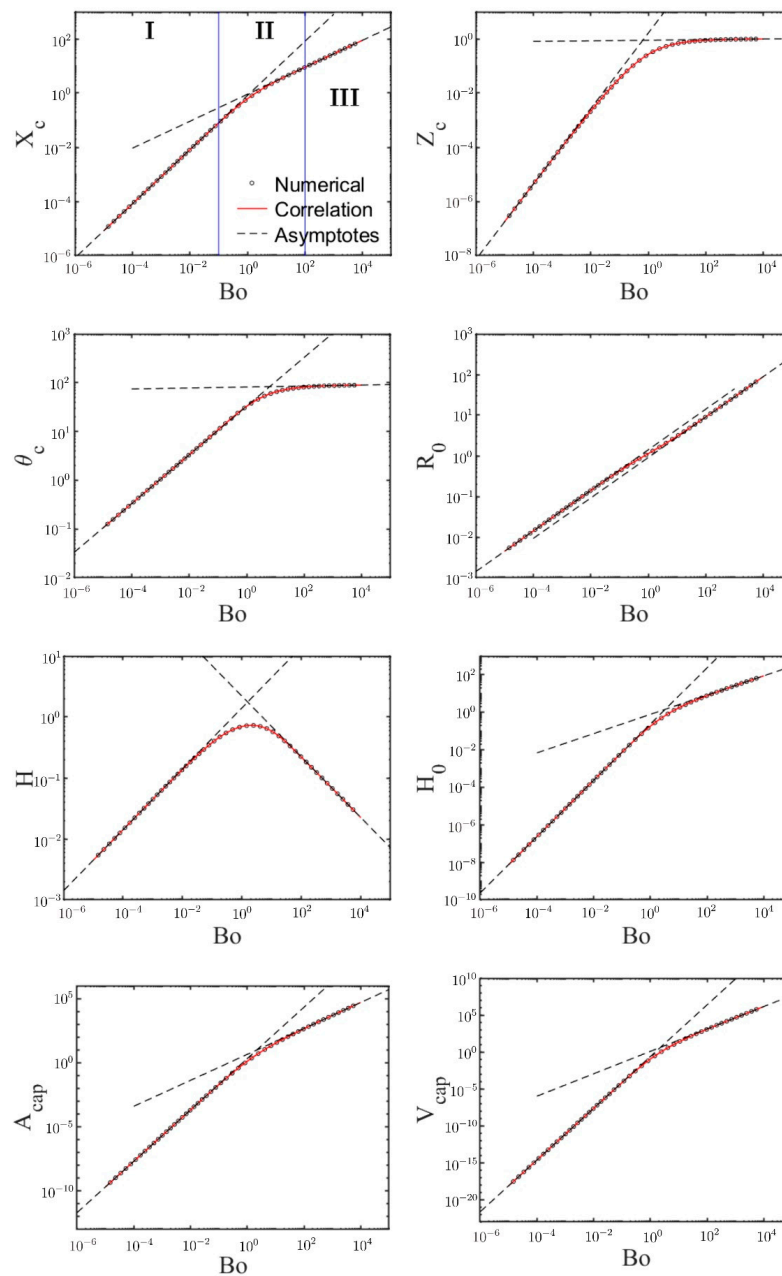

Figure 10. Correlation and two asymptotes of the computed bubble parameters as a function of the Bond number on a log–log scale. The correlation is given by a fifth-order polynomial function in each of the three Bond number regions (I, II, and III). The two asymptotes are given by a power law.

Table 5. Coefficients of the fifth-order polynomial for fitting the bubble parameters.

Parameter	Interval	c_0	c_1	c_2	c_3	c_4	c_5
X_c	$5 \times 10^{-5} < Bo < 0.1$	-0.1735	0.8713	-0.07803	-0.02357	-0.003523	-0.0002078
	$0.1 < Bo < 100$	-0.2107	0.7763	-0.1426	-0.001089	0.02162	-0.004812
	$100 < Bo < 5000$	-0.1349	0.6468	-0.09254	0.02825	-0.004265	0.0002566
Z_c	$5 \times 10^{-5} < Bo < 0.1$	-0.5639	0.6232	-0.3526	-0.09327	-0.01357	-0.000821
	$0.1 < Bo < 100$	-0.5699	0.6353	-0.2707	0.01518	0.02576	-0.006322
	$100 < Bo < 5000$	-0.5019	0.5271	-0.2434	0.06047	-0.007931	0.0004324
θ_c	$5 \times 10^{-5} < Bo < 0.1$	1.561	0.5498	0.02396	0.005715	0.0006714	0.00003092
	$0.1 < Bo < 100$	1.517	0.4145	-0.1141	-0.02333	0.01714	-0.002079
	$100 < Bo < 5000$	1.529	0.4392	-0.1993	0.04873	-0.006298	0.0003392
R_0	$5 \times 10^{-5} < Bo < 0.1$	0.03884	0.3443	-0.08807	-0.02505	-0.003558	-0.000201
	$0.1 < Bo < 100$	0.05469	0.4101	0.00479	0.01815	-0.00413	-0.0004402
	$100 < Bo < 5000$	0.04825	0.3953	0.04915	-0.01243	0.001658	-0.0000919
H	$5 \times 10^{-5} < Bo < 0.1$	-0.1509	0.1079	-0.2103	-0.05746	-0.007922	-0.0004377
	$0.1 < Bo < 100$	-0.1561	0.1188	-0.1691	-0.03095	-0.0007063	0.006116
	$100 < Bo < 5000$	0.2356	-0.3661	-0.0688	0.01897	-0.002739	0.0001626
H_0	$5 \times 10^{-5} < Bo < 0.1$	-0.6643	1.432	-0.0471	-0.01573	-0.002533	-0.000158
	$0.1 < Bo < 100$	-0.7411	1.215	-0.2392	-0.02608	0.03433	-0.005775
	$100 < Bo < 5000$	-0.6902	1.182	-0.319	0.07998	-0.01055	0.0005778
A_{cap}	$5 \times 10^{-5} < Bo < 0.1$	0.1727	1.777	-0.1352	-0.04078	-0.006091	-0.000359
	$0.1 < Bo < 100$	0.1118	1.626	-0.2344	-0.007935	0.0302	-0.006215
	$100 < Bo < 5000$	0.1562	1.578	-0.2698	0.06755	-0.008896	0.0004859
V_{cap}	$5 \times 10^{-5} < Bo < 0.1$	-0.8076	3.187	-0.1962	-0.06074	-0.009259	-0.0005546
	$0.1 < Bo < 100$	-0.9542	2.794	-0.5047	-0.02876	0.07281	-0.01439
	$100 < Bo < 5000$	-0.7944	2.578	-0.525	0.1361	-0.01844	0.001031

Interestingly, X_c can be well expressed even with a single "bending function" for $5 \times 10^{-5} < Bo < 5000$, as given by Equation (29):

$$\log_{10} X_c \approx 0.01864 + \log_{10}\left(\frac{Bo}{1.2787}\right) - 0.4889 \, \log_{10}\left[1 + \left(\frac{Bo}{1.2787}\right)\right]. \qquad (29)$$

The curves fitted by the three fifth-order polynomials and by the single bending function are compared in Figure 11, where both correlations are seen to fit the numerical data well.
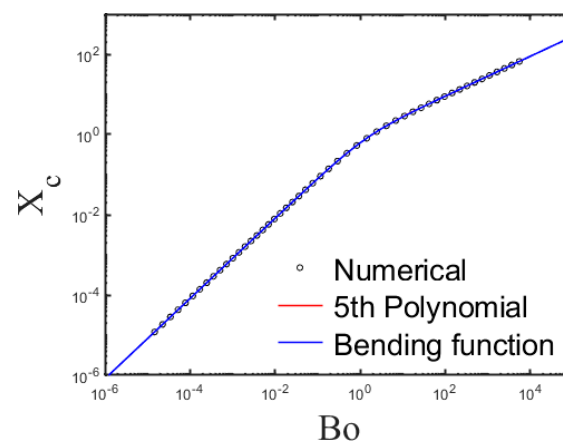

Figure 11. Comparison of the fitting results of the fifth-order polynomials and bending function for X_c.

Two asymptotes appear in Figure 10 as the Bond number goes to zero or infinity. These were obtained numerically via the following simple power law:

$$\Pi \sim a \cdot Bo^b, \tag{30}$$

where the coefficients a and b are shown in Table 6.

Table 6. Coefficients of the power law for asymptotic relations.

Parameter	Limit	a	b
X_c	$Bo \rightarrow 0$	0.8163	1
	$Bo \rightarrow \infty$	0.9063	0.4983
Z_c	$Bo \rightarrow 0$	1.646	1.395
	$Bo \rightarrow \infty$	0.8945	0.01123
θ_c	$Bo \rightarrow 0$	33.09	0.5
	$Bo \rightarrow \infty$	81.56	0.009909
R_0	$Bo \rightarrow 0$	1.414	0.5
	$Bo \rightarrow \infty$	0.9104	0.4978
H	$Bo \rightarrow 0$	1.409	0.4997
	$Bo \rightarrow \infty$	2.197	-0.4978
H_0	$Bo \rightarrow 0$	0.2357	1.5
	$Bo \rightarrow \infty$	0.7787	0.5136
A_{cap}	$Bo \rightarrow 0$	2.094	2
	$Bo \rightarrow \infty$	4.454	1.011
V_{cap}	$Bo \rightarrow 0$	0.2467	3.5
	$Bo \rightarrow \infty$	1.246	1.517

It is noted that R_0 can be rewritten in a more straightforward form as

$$R_0 \sim \sqrt{2Bo} \quad \text{as } Bo \rightarrow 0. \tag{31}$$

Furthermore, the asymptotes can be expressed approximately as a power of $Bo^{1/2}$:

As $Bo \rightarrow 0$, $X_c \approx O(Bo)$, $\theta_c \approx O\left(Bo^{1/2}\right)$, $H \approx O\left(Bo^{1/2}\right)$, $H_0 \approx O\left(Bo^{3/2}\right)$, $A_{cap} \approx O\left(Bo^2\right)$, and $V_{cap} \approx O\left(Bo^{7/2}\right)$.

As $Bo \rightarrow \infty$, $X_c \approx O\left(Bo^{1/2}\right)$, $Z_c \approx O(1)$, $\theta_c \approx O(1)$, $R_0 \approx O\left(Bo^{1/2}\right)$, $H \approx O\left(Bo^{-1/2}\right)$, $H_0 \approx O\left(Bo^{1/2}\right)$, $A_{cap} \approx O(Bo)$, and $V_{cap} \approx O\left(Bo^{3/2}\right)$.

The height of the undisturbed surface above the bubble bottom has a maximum value of $H = 0.7291015$ when $Bo = 4.755563$, as shown in Figure 10.

5. Conclusions

In this study, an improved numerical method was proposed in order to calculate the shape of a floating bubble more precisely and robustly than the conventional method. The proposed method divides the cavity into three parts and accurately finds the location of the connection points at $\varphi = \pi/4$, π, $3\pi/4$, and π by defining specific functions and solving them via the root-finding technique. The type of meniscus was used in order to simplify the conventional bisection method, and the improved method was validated by comparison with previously published numerical and experimental results. The bubble shapes and parameters were then obtained precisely for a more extensive range of Bond numbers ($5 \times 10^{-5} < Bo < 5000$), compared to the previously reported range of Bond numbers ($0.003 < Bo < 241$). The dimensionless maximum depth of submergence of the bubble below the undisturbed liquid surface was determined as $H = 0.7291015$ when $Bo = 4.755563$. The log–log plots of the parameters were divided into three distinct

regions of the Bond number, and each interval was fitted with a fifth-order polynomial function. Interestingly, it was possible to fit the parameter X_c with a single correlation for the entire range of Bond numbers. In addition, the asymptotic relations were presented with a simple power law as the Bond number tended to zero or infinity. Moreover, it was possible to approximate most of the bubble parameters to a power of $Bo^{1/2}$. The correlations and asymptotic equations presented herein are expected to be helpful in scaling models of dynamic bubble-related phenomena such as aerosols and atomization when a bubble bursts.

Institutional Review Board Statement: Not applicable.

Informed Consent Statement: Not applicable.

Data Availability Statement: The data presented in this study are available on request from the corresponding author.

Conflicts of Interest: The author declares no conflict of interest.

Nomenclature

A	dimensionless area of the bubble
B	dimensionless pressure difference across the bottom of the bubble
Bo	Bond number
g	gravitational acceleration, m/s^2
H	dimensionless depth of the bubble below the undisturbed liquid surface
p	pressure, Pa
r_e	equivalent spherical radius of the bubble, m
r_0	radius of the bubble cap, m
r_1, r_2	principal radii of curvature, m
V	dimensionless volume of the bubble
Greek symbols	
α	tangent angle of the meniscus curve
φ	tangent angle of the cavity curve
ρ	density, kg/m^3
σ	surface tension, N/m
Subscripts	
c	the junction point
∞	the point where the meniscus meets the undisturbed liquid surface

References

1. Mason, B.J. The oceans as source of cloud-forming nuclei. *Geofis. Pura E Appl.* **1957**, *36*, 148–155. [CrossRef]
2. Cheng, Y.S.; Zhou, Y.; Irvin, C.M.; Pierce, R.H.; Naar, J.; Backer, L.C.; Baden, D.G. Characterization of marine aerosol for assessment of human exposure to brevetoxins. *Environ. Health Perspect.* **2005**, *113*, 638–643. [CrossRef] [PubMed]
3. Spada, M.; Jorba Casellas, O.; Pérez García-Pando, C.; Janjic, Z.; Baldasano Recio, J.M. Modeling and evaluation of the global sea-salt aerosol distribution: Sensitivity to emission schemes and resolution effects at coastal/orographic sites. *Atmos. Chem. Phys.* **2013**, *13*, 11735–11755. [CrossRef]
4. Dasouqi, A.A.; Yeom, G.S.; Murphy, D.W. Bursting bubbles and the formation of gas jets and vortex rings. *Exp. Fluids* **2021**, *62*, 1–18. [CrossRef]
5. Koch, M.K.; Vossnacke, A.; Starflinger, J.; Schütz, W.; Unger, H. Radionuclide re-entrainment at bubbling water pool surfaces. *J. Aerosol. Sci.* **2000**, *31*, 1015–1028. [CrossRef]
6. Dapper, M.; Wagner, H.J.; Koch, M.K. Assessment of Film Drop Release From Liquid Pools by an Empirical Correlation Approach. *Int. Conf. Nucl. Eng.* **2008**, *48167*, 309–314.
7. Kobayashi, T.; Namiki, A.; Sumita, I. Excitation of airwaves caused by bubble bursting in a cylindrical conduit: Experiments and a model. *J. Geophys. Res. Solid Earth* **2010**, *115*, B10. [CrossRef]
8. Liger-Belair, G.; Cilindre, C.; Gougeon, R.D.; Lucio, M.; Gebefügi, I.; Jeandet, P.; Schmitt-Kopplin, P. Unraveling different chemical fingerprints between a champagne wine and its aerosols. *Proc. Natl. Acad. Sci. USA* **2009**, *106*, 16545–16549. [CrossRef]

9.   Illy, E.; Navarini, L. Neglected food bubbles: The espresso coffee foam. *Food Biophys.* **2011**, *6*, 335–348. [CrossRef]

10.   Bamforth, C.W. The foaming properties of beer. *J. Inst. Brew.* **1985**, *91*, 370–383. [CrossRef]

11.   Hepworth, N.J.; Boyd, J.W.; Hammond, J.R.; Varley, J. Modelling the effect of liquid motion on bubble nucleation during beer dispense. *Chem. Eng. Sci.* **2003**, *58*, 4071–4084. [CrossRef]

12.   Mohammed, H.I.; Giddings, D. Multiphase flow and boiling heat transfer modelling of nanofluids in horizontal tubes embedded in a metal foam. *Int. J. Therm. Sci.* **2019**, *146*, 106099. [CrossRef]

13.   Mohammed, H.I.; Giddings, D.; Walker, G.S.; Talebizadehsardari, P.; Mahdi, J.M. Thermal behaviour of the flow boiling of a complex nanofluid in a rectangular channel: An experimental and numerical study. *Int. Commun. Heat Mass Transf.* **2020**, *117*, 104773. [CrossRef]

14.   Zhang, K.; Li, Y.; Chen, Q.; Lin, P. Numerical study on the rising motion of bubbles near the wall. *Appl. Sci.* **2021**, *11*, 10918. [CrossRef]

15.   Nguyen, C.T.; Gonnermann, H.M.; Chen, Y.; Huber, C.; Maiorano, A.A.; Gouldstone, A.; Dufek, J. Film drainage and the lifetime of bubbles. *Geochem. Geophys. Geosyst.* **2013**, *14*, 3616–3631. [CrossRef]

16.   Chamkha, A.J.; Doostanidezfuli, A.; Izadpanahi, E.; Ghalambaz, M. Phase-change heat transfer of single/hybrid nanoparticles-enhanced phase-change materials over a heated horizontal cylinder confined in a square cavity. *Adv. Powder Technol.* **2017**, *28*, 385–397. [CrossRef]

17.   Ghalambaz, M.; Zadeh, S.M.H.; Mehryan, S.A.M.; Pop, I.; Wen, D. Analysis of melting behavior of PCMs in a cavity subject to a non-uniform magnetic field using a moving grid technique. *Appl. Math. Model.* **2020**, *77*, 1936–1953. [CrossRef]

18.   Yeom, G.S.; Chang, K.S. Two-dimensional two-fluid two-phase flow simulation using an approximate Jacobian matrix for HLL scheme. *Numer. Heat Transf. Part B Fundam.* **2010**, *56*, 372–392. [CrossRef]

19.   Yeom, G.S.; Chang, K.S. A modified HLLC-type Riemann solver for the compressible six-equation two-fluid model. *Comput. Fluids* **2013**, *76*, 86–104. [CrossRef]

20.   Estebe, C.; Liu, Y.; Vahab, M.; Sussman, M.; Moradikazerouni, A.; Shoele, K.; Guo, W. A Low Mach Number, Adaptive Mesh Method for Simulating Multi-phase Flows in Cryogenic Fuel Tanks. In *Thermal and Fluids Analysis Workshop (TFAWS)*; NASA: Washington, DC, USA, 2021.

21.   Hayami, S.; Toba, Y. Drop production by bursting of air bubbles on the sea surface (1) experiments at still sea water surface. *J. Oceanogr. Soc. Jpn.* **1958**, *14*, 145–150. [CrossRef]

22.   Boulton-Stone, J.M.; Blake, J.R. Gas bubbles bursting at a free surface. *J. Fluid Mech.* **1993**, *254*, 437–466. [CrossRef]

23.   Lhuissier, H.; Villermaux, E. Bursting bubble aerosols. *J. Fluid Mech.* **2012**, *696*, 5–44. [CrossRef]

24.   Ghabache, E.; Antkowiak, A.; Josserand, C.; Séon, T. On the physics of fizziness: How bubble bursting controls droplets ejection. *Phys. Fluids* **2014**, *26*, 121701. [CrossRef]

25.   Walls, P.L.; Henaux, L.; Bird, J.C. Jet drops from bursting bubbles: How gravity and viscosity couple to inhibit droplet production. *Phys. Rev. E* **2015**, *92*, 021002. [CrossRef] [PubMed]

26.   Gañán-Calvo, A.M. Revision of bubble bursting: Universal scaling laws of top jet drop size and speed. *Phys. Rev. Lett.* **2017**, *119*, 204502. [CrossRef]

27.   Krishnan, S.; Hopfinger, E.J.; Puthenveettil, B.A. On the scaling of jetting from bubble collapse at a liquid surface. *J. Fluid Mech.* **2017**, *822*, 791–812. [CrossRef]

28.   Bashforth, F.; Adams, J.C. *An Attempt to Test the Theories of Capillary Action by Comparing the Theoretical and Measured Forms of Drops of Fluid*; University Press: Cambridge, UK, 1883.

29.   Toba, Y. Drop production by bursting of air bubbles on the sea surface (II) theoretical study on the shape of floating bubbles. *J. Oceanogr. Soc. Jpn.* **1959**, *15*, 121–130. [CrossRef]

30.   Princen, H.M. Shape of a fluid drop at a liquid-liquid interface. *J. Colloid Sci.* **1963**, *18*, 178–195. [CrossRef]

31.   Medrow, R.A.; Chao, B.T. Floating bubble configurations. *Phys. Fluids* **1971**, *14*, 459–465. [CrossRef]

32.   Bartlett, C.T. Bouncing, Bursting, and Stretching: The Effects of Geometry on the Dynamics of Drops and Bubbles. Ph.D. Dissertation, Boston University, Boston, MA, USA, 2015.

33.   Cohen, C.; Texier, B.D.; Reyssat, E.; Snoeijer, J.H.; Quéré, D.; Clanet, C. On the shape of giant soap bubbles. *Proc. Natl. Acad. Sci. USA* **2017**, *114*, 2515–2519. [CrossRef]

34.   Shaw, D.B.; Deike, L. Surface bubble coalescence. *J. Fluid Mech.* **2021**, *915*, A105. [CrossRef]

35.   Miguet, J.; Rouyer, F.; Rio, E. The Life of a Surface Bubble. *Molecules* **2021**, *26*, 1317. [CrossRef] [PubMed]

36.   Puthenveettil, B.A.; Saha, A.; Krishnan, S.; Hopfinger, E.J. Shape parameters of a floating bubble. *Phys. Fluids* **2018**, *30*, 112105. [CrossRef]

37.   Teixeira, M.A.; Arscott, S.; Cox, S.J.; Teixeira, P.I. What is the shape of an air bubble on a liquid surface? *Langmuir* **2015**, *31*, 13708–13717. [CrossRef]

38.   Lohnstein, T. Zur Theorie des Abtropfens mit besonderer Rücksicht auf die Bestimmung der Kapillaritätskonstanten durch Tropfversuche. *Ann. Phys.* **1906**, *325*, 237–268. [CrossRef]

39.   Yeom, G.S. Comparison of the shapes of isovolumetric bubbles floating on various liquids. *J. Comput. Fluids Eng.* **2021**, *26*, 77–83. (In Korean) [CrossRef]

40.   Freud, B.B.; Freud, H.Z. A theory of the ring method for the determination of surface tension. *J. Am. Chem. Soc.* **1930**, *52*, 1772–1782. [CrossRef]

41.   Dormand, J.R.; Prince, P.J. A family of embedded Runge-Kutta formulae. *J. Comput. Appl. Math.* **1980**, *6*, 19–26. [CrossRef]
42.   Brakke, K.A. The surface evolver. *Exp. Math.* **1992**, *1*, 141–165. [CrossRef]